

Cite this: *J. Mater. Chem. A*, 2025, 13, 41903

Alkali triel chalcogenide nanocrystals: a molecular reactivity approach to ternary phase selectivity

Md Riad Sarkar Pavel,^a Anuluxan Santhiran,^{ID} ^{ab} Seth Dalberg,^a Aaron J. Rossini ^{ID} ^{ab} and Javier Vela ^{ID} ^{*ab}

Alkali-metal-based materials are promising building blocks for energy conversion and storage technologies. Here, we use a molecular reactivity-based solution-phase approach to selectively synthesize multiple phases and specific polymorphs of lithium- and sodium-containing triel chalcogenide nanocrystals, LiTrCh_2 , NaTrCh_2 , and NaTr_3Ch_5 , where $\text{Tr} = \text{Ga}$ and In and $\text{Ch} = \text{S}$, Se , and Te . Analogous to the case of binary II–VI and III–V tetrahedral semiconductors, where the two commonly isolated zinc blende and wurtzite polymorphs are separated by only 1–50 meV f.u.⁻¹, we find that LiTrCh_2 nanocrystals easily adopt tetragonal (chalcopyrite) and orthorhombic polymorphs separated by only 2.7–6.2 meV f.u.⁻¹. Because of this small energy difference, soft colloidal synthesis succeeds in accessing either one of these polymorphs, depending on the specific dichalcogenide precursor used. Highly reactive diethyl diselenide favors the thermodynamically more stable tetragonal $\bar{I}42d$ phase, whereas mildly reactive diphenyl diselenide favors the kinetic, metastable orthorhombic $Pna2_1$ phase. Density functional theory calculations confirm the relative energies among multiple LiTrCh_2 polymorphs and also model the observed powder X-ray diffraction pattern of a new $\text{C2 NaIn}_3\text{Te}_5$ phase. ⁷Li, ⁶⁹Ga, and ⁷⁷Se solid-state NMR spectra are consistent with phase-pure ternary LiGaSe_2 nanocrystals. A majority of the nanocrystal compositions are visible-light emitters. This work opens the door to new Li/Na-based ternary triel chalcogenide nanostructures for energy storage and conversion applications.

Received 29th September 2025
Accepted 6th November 2025

DOI: 10.1039/d5ta07992f

rsc.li/materials-a

Introduction

From their discovery in 1807 (ref. 1) to the next generation of batteries^{2–4} and solar cells,⁵ alkali metals have become indispensable elements at the forefront of research and development in new energy conversion and storage materials and devices. Alkali ion batteries provide on-demand power to small portable electronics and electric vehicles.⁶ High energy density, light-weight Li batteries are most widespread.^{7,8} Similarly, Na and K batteries continue to gain momentum due to their wide elemental geodistribution, low potential, fast ion diffusion, and low toxicity compared to Pb acid batteries.^{9,10} Alkali metal chalcogenides have shown promise beyond battery anodes,¹¹ for example, as earth-abundant, environmentally benign, and biocompatible materials for photovoltaic devices.¹² By mitigating adverse interfacial recombination pathways, alkali ions help to effectively reduce photovoltaic losses and increase the open-circuit current and fill factor of perovskite¹³ and copper indium gallium diselenide (CIGS) solar cells.¹⁴

In this context, alkali triel chalcogenides ($\text{Alk-III}_x\text{-VI}_y$; $\text{Alk} = \text{Li}$, Na , and K ; $\text{III} = \text{Ga}$ and In ; $\text{VI} = \text{S}$, Se , Te , etc.) belong to an

interesting family of ternary semiconductors with rich structural chemistry and useful optoelectronic properties. While related I–III–VI₂ materials (*i.e.* CuInSe_2 , AgGaSe_2 , etc.) adopt the chalcopyrite structure ($\bar{I}42d$), lithium triel chalcogenides (Li-III-III-VI_2) crystallize in a wide range of space groups. Depending on their composition and specific crystallization conditions,

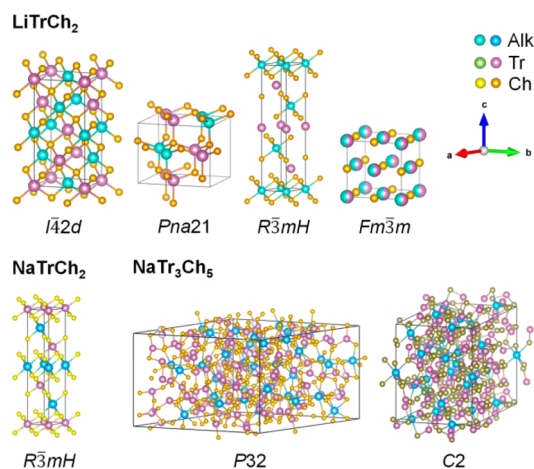


Fig. 1 Common crystal structures of ternary lithium- and sodium-based triel chalcogenide semiconductors.

^aDepartment of Chemistry, Iowa State University, Ames, Iowa 50011, USA. E-mail: vela@iastate.edu

^bAmes National Laboratory, Ames, Iowa 50011, USA



they can adopt orthorhombic ($Pna2_1/P2_1nb$), cubic ($Fm\bar{3}m$), and trigonal ($R\bar{3}mH$) phases.¹² (Fig. 1). In turn, sodium triel chalcogenides ($Na-III_x-VI_y$, $x = 1, 3$, $y = 2, 5$) adopt mainly trigonal ($R\bar{3}mH/P32$) or monoclinic ($C2$) phases, with some tetragonal and orthorhombic variations. From a colloidal synthesis perspective, this polymorphism offers an opportunity to observe, study, and isolate metastable or kinetic phases with unprecedented chemical and physical properties.^{15,16} From the perspective of applications, replacement of Cu or Ag with Li widens the semiconducting band gap, increasing the threshold for laser-induced damage and overall photostability. Thus, in addition to batteries or solar cells,¹⁷ alkali triel chalcogenides may be useful in near- and mid-IR nonlinear optics,^{18–20} water splitting²¹ and CO₂ photocatalysis,²² and also in neutron detectors,²³ and even phase-change memory materials.²⁴ Already, experimental examples underscoring the potential of this new family of nanostructured materials include the use of LiInS₂ or LiInSe₂ nanosheets in batteries,^{25,26} NaGaS₂ in radiation detectors,²⁷ and KGaS₂ nanocrystals in the conversion of CO₂ to CO.²⁸

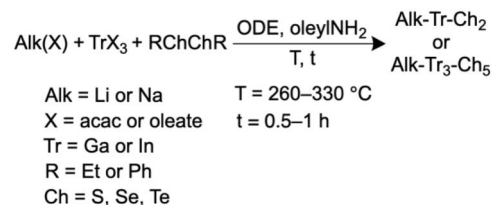
Common approaches to achieve synthetic control during nanocrystal preparations include optimization of reaction conditions (reaction time, temperature), as well as utilization of different ligands and solvents.^{29,30} A powerful tool in nanocrystal synthesis is leveraging predictable trends in the reactivities of molecular precursors based on their molecular structure, in order to control the kinetics of nanocrystal nucleation and growth.^{31,32} Disubstituted (diorganyl) dichalcogenides (RChChR; R = ethyl, methyl, phenyl, *etc.*; Ch = S, Se, *etc.*) are prime examples of this approach because their reactivities strongly depend on the identity of the organic substituent (R).^{33–36} In this way, different dichalcogenide precursors can enable the preparation of metastable phases depending on their C–Ch bond dissociation energies.³¹

At present, high-temperature reactions between the elements result in bulk (polycrystalline) or single crystals of alkali triel chalcogenides. A few solvothermal and molten-salt syntheses,³⁷ as well as high-temperature reactions in flux, also produce alkali triel chalcogenides with large particle size, although binary impurities are sometimes present.^{38–40} A few colloidal syntheses of (Alk)–Tr–Ch₂ nanocrystals have appeared recently.^{41–43} Interestingly, only pressure-induced Alk–III–VI₂ phase transformations are reported.⁴⁴ Here, we describe a molecular reactivity approach to the phase-selective synthesis of lithium- and sodium-based alkali triel chalcogenide (Ch = S, Se, and Te) nanocrystals using readily available alkali metal, triel, and disubstituted dichalcogenide RChChR precursors.

Results and discussion

Colloidal alkali triel chalcogenide nanocrystals

Reaction of Li(acac) and Ga(acac)₃ or In(acac)₃ with disubstituted dichalcogenides (RChChR) in oleylamine (oleylNH₂) and 1-octadecene (ODE) at 270–330 °C produces LiTrCh₂ nanocrystals (Scheme 1). Because of its mild reactivity and moderate solubility, Li(acac) is more reliable and versatile than other Li precursors, such as nitrates, halides, or carbonates.⁴⁵ Harsher



Scheme 1 Solution-phase synthesis of colloidal alkali triel chalcogenide nanocrystals.

precursors such as LiH, Li(NPr₂), PhLi, or *n*-BuLi react too fast under these conditions, resulting in lower order, binary triel chalcogenides (Tr₂Ch₃) rather than the desired ternary nanocrystals.

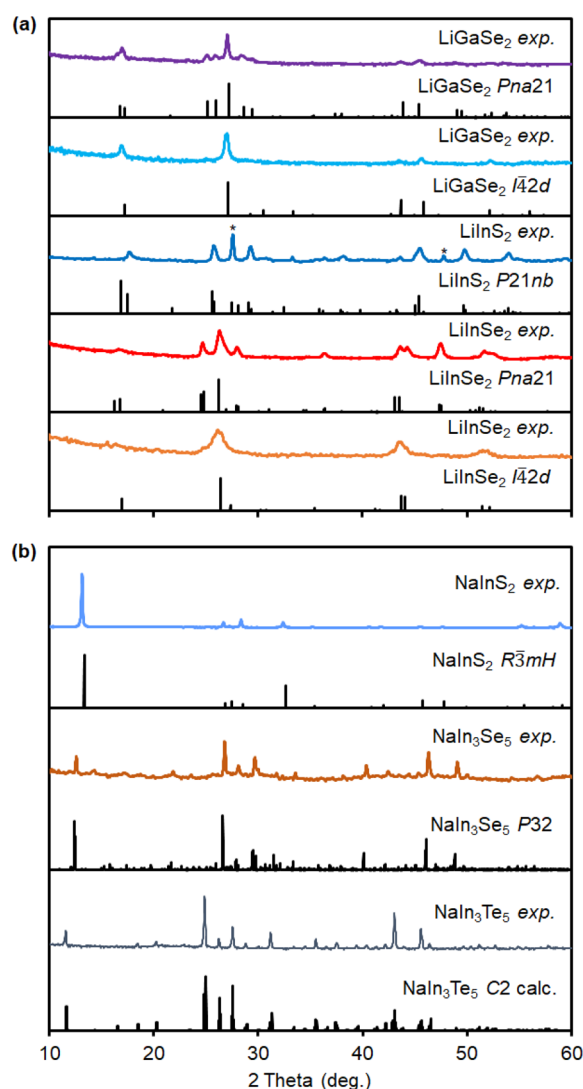


Fig. 2 Powder XRD of (a) $Pna2_1$ LiGaSe₂ (ICSD-53093), $I42d$ LiGaSe₂ (ICSD-89176), $P2_1nb$ LiInS₂ (ICSD-53093), $Pna2_1$ LiInSe₂ (ICSD-60838), and $I42d$ LiInSe₂ (ICSD-56532) nanocrystals; (b) $R\bar{3}mH$ NaInS₂ (ICSD-25557), $P32$ NaIn₃Se₅ (ICSD-243563), and $C2$ NaIn₃Te₅ nanocrystals (calculated using VASP, see Methods). *In₂S₃ impurity (ICSD-23844).



The experimental powder X-ray diffraction (XRD) patterns of the nanocrystals match the reported $Pna2_1$ and $I\bar{4}2d$ (LiGaSe_2 and LiInSe_2) or $P2_1nb$ (LiInS_2) phases of these materials (Fig. 2). The specific polymorph observed is highly dependent on the structure and reactivity of the specific disubstituted dichalcogenide precursor used—see further phase selectivity and computations sections below. The single crystalline domain (Scherrer) sizes calculated from the powder XRD peak widths for LiTrCh_2 nanocrystals range from 7 to 20 nm, respectively (Table 1).

Using a similar approach, the reaction of Na(oleate) with In(acac)_3 and PhChChPh ($\text{Ch} = \text{S}, \text{Se}, \text{Te}$) enables the preparation of nanocrystalline sodium triel chalcogenides. Powder XRD patterns match those reported for $R\bar{3}mH$ NaInS_2 , $P32$ NaIn_3Se_5 and—for the first time—a previously unreported $C2$ NaIn_3Te_5 phase (Fig. 2). This new ternary compound has a relatively large monoclinic unit cell comprised of octahedral $[\text{NaTe}_6]$, tetrahedral $[\text{InTe}_4]$, and four-coordinate $[\text{Na}_2\text{SeIn}_2]$ sites (see the SI). Rietveld refinement of the experimental powder XRD pattern matches well with the calculated $C2$ XRD (see calculations below). The higher reactivity of Na(oleate) compared to Li(acac) results in generally larger 510–960 nm particles for Na- vs. Li-based materials (Table 1).

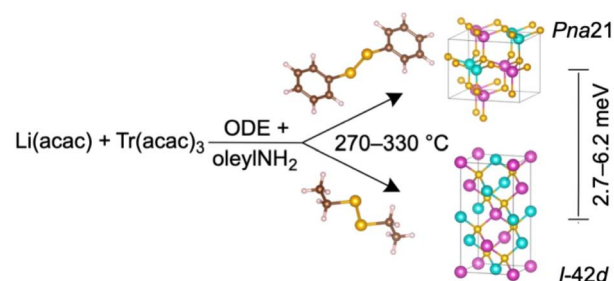
Phase selectivity and morphology

The colloidal LiTrCh_2 nanocrystals made by our method typically adopt the tetragonal $I\bar{4}2d$ chalcopyrite and/or orthorhombic $Pna2_1$ (LiTrSe_2) and the $P2_1nb$ (LiInS_2) structures (Table 1). This agrees with our calculations showing that these two phases have very similar energies. In the case of LiGaSe_2 and LiInSe_2 , the chalcopyrite ($I\bar{4}2d$) polymorph is the most thermodynamically stable, but only by about 2.7–6.2 meV compared to the orthorhombic ($Pna2_1$) phase (see computations below). For comparison, the two most isolated, zinc blende and wurtzite polymorphs of binary tetrahedral semiconductors (II–VI, III–V) are only 1–50 meV per formula unit (f.u.) apart.^{46,47}

To effectively deliver chalcogen to the reaction medium, both of the C–Ch and Ch–Ch bonds in the dichalcogenide precursor must break. Aromatic disubstituted dichalcogenides such as PhChChPh have strong C(Aryl)–Ch bonds (64.4–

69.8 kcal mol⁻¹) and weak Ch–Ch bonds (43.6–45.7 kcal mol⁻¹, as judged by their bond dissociation energies).³¹ As a result, PhChChPh precursors release $[\text{Ch}]$ very slowly but quickly release $[\text{PhCh}\cdot]$; these can act as surface passivating agents that stabilize small reactive clusters and seeds, slowing nanocrystal growth. Therefore, the use of aryl-substituted dichalcogenides, such as PhSeSePh , enables the preparation of metastable, kinetic orthorhombic ($Pna2_1$) polymorphs of LiGaSe_2 and LiInSe_2 (Scheme 2 and Table 1). These observations agree with the isolation of metastable polymorphs of CuInSe_2 —and, very recently, CsGaCh_2 —from reactions using PhSeH ³⁵ and PhSeSePh ,⁴³ respectively, both of which bear strong, hard-to-break C–Se bonds.

In contrast, aliphatic substituted dichalcogenides have much weaker C–Ch bonds (by about 11–12 kcal mol⁻¹),³¹ compared to those bearing aromatic substituents. Consequently, both C–Ch and Ch–Ch bonds in EtChChEt precursors break more easily, releasing $[\text{Ch}]$ relatively fast and accelerating the rates of nucleation and growth. Thus, the use of the much more reactive EtSeSeEt precursor results in the isolation of the more stable, thermodynamic chalcopyrite ($I\bar{4}2d$) polymorphs of LiGaSe_2 and LiInSe_2 (Scheme 2). Using PhSSPh also results in the formation of the orthorhombic ($P2_1nb$) phase of LiInS_2 , the only experimentally reported polymorph for this material, albeit with a small binary In_2S_3 impurity (Table 1). To further increase the phase purity of LiInS_2 , future work will explore the use of precursors with weaker C–S bonds compared to that of PhSSPh . Alternatively, more reactive Li precursors could also decrease



Scheme 2 Phase-selective synthesis of colloidal LiTrCh_2 nanocrystals.

Table 1 Synthesis of ternary alkali triel chalcogenide nanocrystals

Precursors (mmol)			Conditions ^a		Products	
Alkali metal	Triel	Chalcogen	T (°C)	t (min)	Phase	Scherrer, TEM/SEM (nm)
Li(acac) (0.1)	Ga(acac)_3 (0.1)	PhSeSePh (0.2)	330	60	$Pna2_1$ LiGaSe_2	15 ± 4.9 , 11 ± 4.2
Li(acac) (0.1)	Ga(acac)_3 (0.1)	EtSeSeEt (0.6)	300	60	$I\bar{4}2d$ LiGaSe_2	20 ± 5.5 , 22 ± 5.6
Li(acac) (0.15)	In(acac)_3 (0.2)	PhSSPh (0.6)	330	60	$P2_1nb$ LiInS_2 + In_2S_3 ^b	8.1 ± 1.3
Li(acac) (0.1)	In(acac)_3 (0.1)	PhSeSePh (0.2)	270	60	$Pna2_1$ + $I\bar{4}2d$ (4 : 1) ^c LiInSe_2	18 ± 8.3 , 13 ± 6.7
Li(acac) (0.1)	In(acac)_3 (0.1)	EtSeSeEt (0.4)	270	60	$I\bar{4}2d$ LiInSe_2	7.4 ± 1.6 , 19 ± 5.5
Na(oleate) (0.1)	In(acac)_3 (0.1)	PhSSPh (0.2)	280	30	$R\bar{3}mH$ NaInS_2	507 ± 83
Na(oleate) (0.1)	In(acac)_3 (0.1)	PhSeSePh (0.1)	290	60	$P32$ NaIn_3Se_5	957 ± 182
Na(oleate) (0.1)	In(acac)_3 (0.1)	PhTeTePh (0.05)	260	30	$C2$ NaIn_3Te_5	946×256 ^d

^a 4 mL ODE + 4 mL oleylNH_2 . ^b Minor impurity. ^c Estimated from match. ^d Total span \times arm width of hexapods.



the amount of In_2S_3 byproduct by virtue of releasing Li much faster into the reaction mixture.

Bright-field transmission electron microscopy (TEM) shows that the morphology of LiTrCh_2 nanocrystals mainly depends on their composition rather than on the specific polymorph present. For example, both $Pna2_1$ and $I42d$ LiGaSe_2 nanocrystals are spheroidal, even though high-resolution (HR) TEM and fast Fourier transform (FFT) of selected area electron diffraction (SAED) patterns confirm the presence of different sets of planes for the $Pna2_1$ [(110), (221)] and $I42d$ [(112), (101), (204)] phases, as shown in Fig. 3a and b, respectively. $P2_1nb$ LiInS_2 nanocrystals are also spheroidal (see SI). In contrast, both $Pna2_1$ and $I42d$ LiInSe_2 nanocrystals adopt a triangular plate morphology, even though HR TEM and FFT SAED analyses confirm the presence of different sets of planes for the $Pna2_1$ [(002), (210), (113), and (231)] and $I42d$ [(112), (103), and (204)] phases, as shown in Fig. 3c and d, respectively. Energy dispersive X-ray spectroscopy (EDS) under scanning electron microscopy (SEM) is consistent with the nanocrystals' compositions; for example, $(\text{Li})\text{Ga}_{1.0}\text{Se}_{2.4}$ and $(\text{Li})\text{In}_{1.0}\text{Se}_{1.9}$ for the $Pna2_1$ phases of LiGaSe_2 and LiInSe_2 , respectively (the light Li atoms are not detected).

Interestingly, the fact that LiGaSe_2 and LiInS_2 nanocrystals are spheroidal while LiInSe_2 nanocrystals containing the heavier Se chalcogen are highly anisotropic (plate-like) has some precedence in the literature. For example, NaSbSe_2 nanocrystals are quasispheroidal while NaBiSe_2 nanocrystals

are anisotropic (elongated, rods).^{48,49} Particle shapes with lower aspect ratios are normally preferred thermodynamically.⁴⁹ In our case, the less reactive, lighter Ga and S precursors required significantly higher reaction temperatures (300–330 °C, Table 1) compared to the more reactive, Se precursors (270 °C), which likely explains why the former trended toward the lower aspect ratio, spheroidal shapes.

SEM images reveal that NaInS_2 , NaIn_3Se_5 , and NaIn_3Te_5 nanocrystals adopt different morphologies (Fig. 4 and SI). Very much like the Li-ternary nanocrystals, Na-containing ternary nanocrystals undergo shape evolution from lower to higher anisotropy on going down the chalcogen group from S to Se to Te. Specifically, NaInS_2 crystals are spheroidal, NaIn_3Se_5 crystals exhibit some anisotropy and are cuboidal, and NaIn_3Te_5 crystals are very anisotropic and adopt a hexapod-like shape. Thus, the idea that composition plays a key role in determining the shape of Li- and Na-containing ternary chalcogenide nanocrystals is strongly supported by the available data. Nanocrystals containing lighter atoms often adopt more thermodynamically favorable, isotropic shapes, while those containing heavier atoms tend to be much more anisotropic. Recent reports on AlInSe_2 (A = K, Rb, Cs) nanocrystals also showed a variety of morphologies depending on the different cations that were present and the chalcogen precursors used.⁴¹ Selected EDS area scans under the SEM show average compositions of $\text{Na}_{1.2}\text{In}_{1.0}\text{S}_{2.0}$, $\text{Na}_{1.4}\text{In}_{3.0}\text{Se}_{5.1}$, and $\text{Na}_{4.5}\text{In}_{2.5}\text{Te}_{5.0}$ (see SI). An excess of Na and Ch atoms in the latter may be attributed to some remaining unreacted sodium precursor or amorphous impurity, as it is absent in the powder XRD.

Stability and phase transformations

The phase-selective synthesis and structural transformations of alkali metal-based ternary chalcogenides continue to be the subject of intense research activity. For example, CsGaCh_2 (Ch = S, Se) adopts a TlGaSe_2 -type ($mC64$) layered (2D) structure at low temperature and a KFeS_2 -type ($mC16$) structure containing one-dimensional (1D) chains at high temperature. Density functional theory (DFT) calculations show these two polymorphs are only 0.01 eV per atom apart.⁴² In the bulk, $mC64$ CsGaCh_2 reversibly phase transitions to the $mC16$ polymorph at ~600 °C. At the nanoscale, $mC64$ CsGaCh_2 irreversibly converts to the thermodynamic $mC16$ polymorph at 320 °C in solution⁴³ and at 1000 °C in the solid state.⁴²

In this work, we find that LiTrCh_2 nanocrystals possess significant air and thermal stability, as evidenced by continued monitoring of their powder XRD over time and by thermal analyses (see SI). Notably, LiInSe_2 nanocrystals remain phase

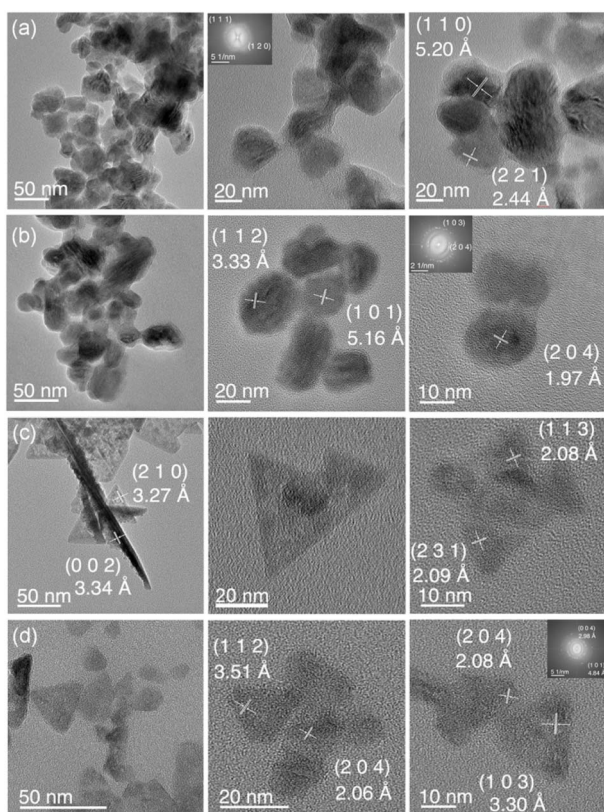


Fig. 3 Representative TEM images of (a) $Pna2_1$ LiGaSe_2 (TEM particle size: 10 ± 4.2 nm), (b) $I42d$ LiGaSe_2 (22 ± 5.6 nm), (c) $Pna2_1$ LiInSe_2 (13 ± 6.7 nm), and (d) $I42d$ LiInSe_2 (19 ± 5.5 nm) nanocrystals.

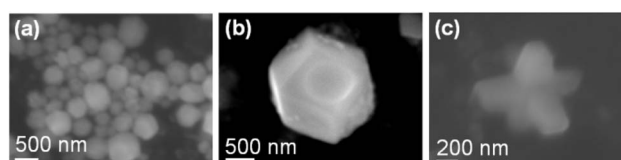


Fig. 4 Representative SEM images of (a) NaInS_2 , (b) NaIn_3Se_5 , and (c) NaIn_3Te_5 nanocrystals.



pure even after 5 months under ambient conditions of temperature and air, while LiGaSe₂ nanocrystals only start showing signs of partial decomposition to lower order, binary impurities after 2 months. Both are remarkably thermally stable in N₂, losing ≤3% mass to 1000 °C.

SSNMR spectroscopy

Solid-state NMR (SSNMR) spectroscopy experiments were performed on ternary LiGaSe₂ and LiInSe₂ samples to identify their chemical environments. ⁷Li is a spin 3/2 nucleus with 92.4% natural abundance.⁵⁰ ⁷Li has a chemical shift of 1 ppm and 3 ppm for the LiGaSe₂ and LiInSe₂, respectively, differing by 2 ppm (Fig. 5a). ⁶⁹Ga is a spin 3/2 nucleus with 60.1% natural abundance.⁵⁰ Quadrupolar nuclei, such as ⁶⁹Ga, often have sizable first- and second-order quadrupolar interactions, which lead to broader central transition SSNMR spectra.^{51,52} The static ⁶⁹Ga SSNMR spectrum was acquired with a wideband uniform rate smooth truncation QCPMG (WCPMG) pulse sequence.^{53,54} The WCPMG echoes were coadded using a C code to make the coadded echo SSNMR spectrum (Fig. 5b). The electric field gradients (EFG) tensor parameters were measured by fitting the coadded SSNMR spectrum, summarized in Table 2. ⁷⁷Se is a spin 1/2 nucleus with 7% natural abundance.⁵⁰ Most ⁷⁷Se compounds have large spin-lattice relaxation rates (*T*₁), which results in a longer experimental time.^{55,56} The MAS ⁷⁷Se NMR spectrum of LiGaSe₂ was acquired using a Carr-Purcell Meiboom-Gill (CPMG) pulse sequence. The ⁷⁷Se SSNMR spectrum shows a single peak that has an isotropic chemical shift (*d*_{iso}) of 794 ppm with a span (*W*) of ~475 ppm.

Optical properties

The band gaps of 1.8–3.4 eV in the synthesized LiTrCh₂ nanocrystals closely match the values reported in the literature^{57,58} (Table 3). It is noteworthy that, despite their distinct structures, the tetragonal (*I42d*) and orthorhombic (*Pna2*₁) forms of LiTrCh₂ have similar band gaps, which is consistent with previous reports on single crystals.⁵⁹ All LiTrCh₂ nanocrystals

Table 2 EFG/chemical shift tensors of LiGaSe₂ nanocrystals

Material	Nuclei	δ_{iso} (ppm)	Ω (ppm)	κ	η_{Q}	C_{Q} (MHz)
LiGaSe ₂	⁶⁹ Ga	233	—	—	1.0	4.9
	⁷⁷ Se	794	473	0.2	—	—

display UV or Vis photoluminescence, with maxima (PL_{max}) between 380 nm and 620 nm, and quantum yields (QY) ranging from 1.2–4.6% (Fig. 6).

Multiple literature reports indicate that the band gap and PL_{max} of LiTrCh₂ semiconductors are strongly dependent on defects.⁶⁰ For example, LiInSe₂ has an intrinsic bandgap of around 2.8 eV,⁶¹ but this narrows with increasing defect density.^{62,63} Density functional theory (DFT) calculations suggest that In_{Li} and Li_{In} antisites are the main defects responsible for this behavior.⁶³ Defect types in yellow single crystals of Li_{1.01}In₁Se₂ are V_{Se}⁺ and Li_{In}²⁻, while those in red crystals are In_{Li}²⁺ and V_{Li}⁻.²³ In this study, we observe that the *Pna2*₁ and *I42d* phases of LiInSe₂ have band gaps of 1.8 and 2.0 eV. Thus, we assume that both synthesized nanocrystals possess defects to some degree, with a higher density in the *Pna2*₁ LiInSe₂ nanocrystals. Further work will address ways to decrease the number of defects as a way to further increase the PL QYs of these materials.

Sodium-based ternary nanocrystals, on the other hand, have band gaps of 1.7–2.5 eV (see SI). Importantly, NaInS₂ and NaIn₃Se₅ nanocrystals show visible-range PL, while NaIn₃Te₅ lacks PL in either Vis or NIR regions. Previously, NaInS₂ nanoplates and NaIn₃Se₅ single crystals showed band gaps of 2.35 eV (ref. 64) and 2.17 eV,⁴⁰ respectively.

Correlating theory and experiment

Seeking to obtain deeper physical insight into our results, we used the Vienna *Ab initio* Simulation Package (VASP)⁶⁵ and the Tight Binding Linear Muffin-tin Orbital Atomic Sphere

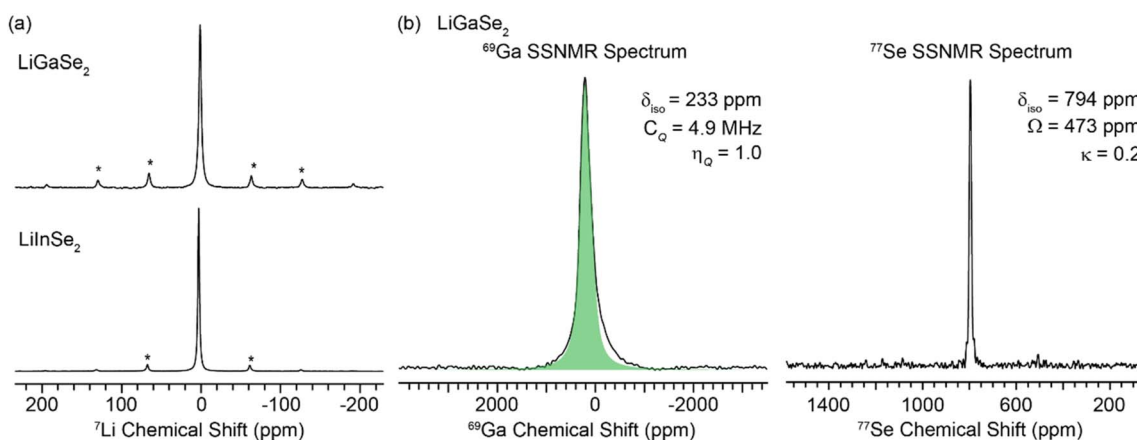


Fig. 5 (a) Comparison of ⁷Li spin-echo SSNMR spectra of LiGaSe₂ and LiInSe₂ nanocrystals. The MAS frequency was 10 kHz. Spinning side bands are marked with an asterisk. (b) Static ⁶⁹Ga WCPMG SSNMR spectrum and MAS ⁷⁷Se CPMG SSNMR spectrum of LiGaSe₂ nanocrystals. The MAS frequency was 22 kHz.



Table 3 Optical properties of alkali triel chalcogenides

Nanocrystal phase	Band gap (eV)			
	Exp.		Theo.	
	(Abs.)	Lit.	(DFT)	Lit.
<i>Pna2</i> ₁ LiGaSe ₂	3.0	2.1–3.7	2.0–2.1	2.4–3.4
<i>I</i> $\bar{4}2d$ LiGaSe ₂	2.7	1.7–2.0	2.0	2.8
<i>P2</i> ₁ <i>nb</i> LiInSe ₂	3.4	3.6	2.1	1.3–3.3
<i>Pna2</i> ₁ LiInSe ₂	1.8	1.6–2.8	1.5–1.6	2.6
<i>I</i> $\bar{4}2d$ LiInSe ₂	2.0	2.9	1.5–1.6	—
<i>R</i> $\bar{3}mH$ NaInSe ₂	2.5	2.4	—	0.7–3.3
<i>P32</i> NaIn ₃ Se ₅	2.1	2.2	—	—
<i>C2</i> NaIn ₃ Te ₅	1.7	—	0.6	—

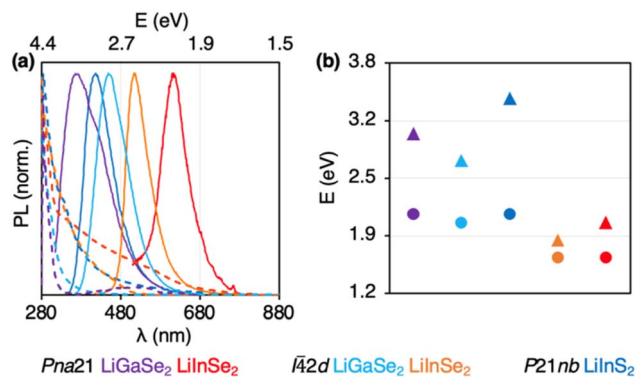


Fig. 6 (a) Optical absorption (dashed lines) and photoluminescence (solid lines) of LiTrCh₂ nanocrystals. (b) Experimental (▲) vs. calculated (●) band gaps.

Approximation (TB-LMTO-ASA)⁶⁶ to estimate the relative energies, bonding, and optical properties of all phases for each LiTrCh₂ composition. We used coloring patterns^{16,67,68} for phases with mixed-cation sites (below).

VASP and LMTO calculations show direct band gaps in the range of 1.5–2.1 eV for these LiTrCh₂ nanocrystals and a small theoretical band gap of 0.6 eV for the hypothetical *C2* NaIn₃Te₅ (Table 3). These band gaps are underestimated by 20–54% compared to the experimentally observed values (Fig. 6). Such underestimation is common in semiconductor chalcogenides because the excited states are not considered in the DFT calculations.⁶⁹ Density of states (DOS) shows that the Ch-p orbital dominates the valence bands, with some contributions from the Tr-s and Tr-p orbitals in all the phases (see SI). Previous DFT calculations on LiTrCh₂ and NaTrCh₂ also indicated a substantive contribution of the covalent component from the Ch-p and Tr-p orbitals in the chemical bonding of these materials.^{70–72}

A comparison of relative energies among the PBE-relaxed crystal structures for each composition yields useful insights into the outcome of our nanocrystal preparations. LiGaSe₂ has two reported phases, *I* $\bar{4}2d$ and *Pna2*₁, which are only 6.2 meV apart, with *I* $\bar{4}2d$ being the lowest energy polymorph.⁷³ As noted above, this explains our ability to prepare either phase

selectively using molecular precursors with different reactivity. More specifically, the more reactive EtSeSeEt leads to the quick formation of nanocrystals adopting the thermodynamic *I* $\bar{4}2d$ phase, while the relatively mildly reactive PhSeSePh enables the isolation of nanocrystals adopting the kinetic (metastable) *Pna2*₁ phase (Scheme 2). In contrast, LiInSe₂ has only one crystallographically reported phase, *P2*₁*nb*, as observed experimentally.

The inorganic crystal structure database (ICSD) contains four reported polymorphs for LiInSe₂, including a disordered cubic *Fm* $\bar{3}m$ phase with mixed cation (Li/In) sites. In this case, we first created two different supercells using different coloring patterns while keeping the stoichiometry intact,⁶⁷ which we labeled (*Fm* $\bar{3}m$)S1 and (*Fm* $\bar{3}m$)S2 (Fig. 7). As in the case of the lighter, gallium-containing analogue, *I* $\bar{4}2d$ LiInSe₂ has the lowest energy, followed closely by *Pna2*₁ LiInSe₂, which is only *ca.* 2.7 meV higher than the first. Interestingly, the even smaller energy difference compared to the previous gallium case explains why it is even more challenging in the indium case to isolate metastable *Pna2*₁ LiInSe₂ nanocrystals in 100% pure form (Table 1).

The other polymorphs of LiInSe₂, including *R* $\bar{3}mH$ (291 meV higher), and the colored supercells (*Fm* $\bar{3}m$)S1 and (*Fm* $\bar{3}m$)S2 (715–732 meV higher), contain octahedrally coordinated cation sites and shorter bonds. These high-pressure phases, which are metallic in character (see SI), are too high-energy to be relevant under the relatively low temperature and ambient pressure, colloidal synthesis conditions used here. Lastly, because the ICSD lacks a reported structure for NaIn₃Te₅, we

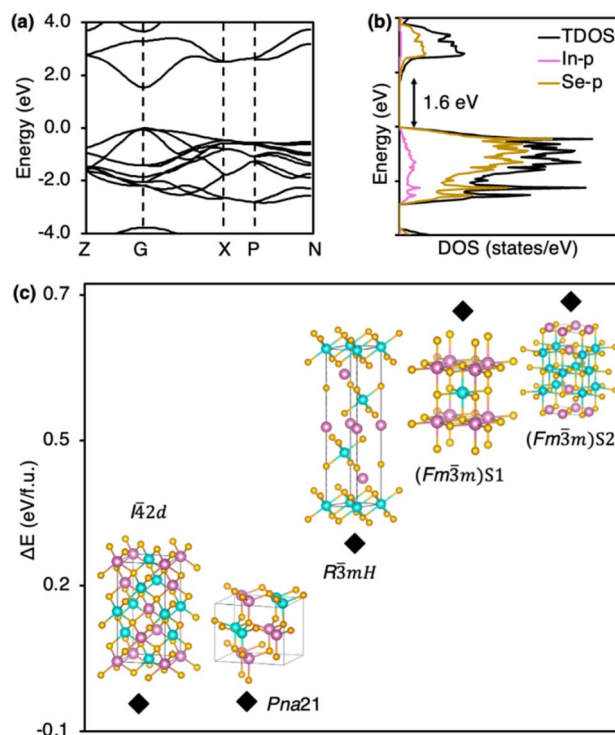


Fig. 7 Calculated (a) band structure and (b) density of states for *I* $\bar{4}2d$ LiInSe₂, along with (c) relative energies for its different polymorphs.



computationally built a unit cell by replacing Ga with In in the reported *R32H* crystal structure of NaGa_3Te_5 . The calculated XRD pattern matches well with the powder XRD pattern obtained experimentally (Fig. 2b).

Conclusions

In summary, we have synthesized eight different polymorphs of Li/Na-based ternary chalcogenide nanocrystals using a reliable colloidal synthesis method. A combination of powder XRD, high-resolution (HR) TEM, fast Fourier transform (FFT) of selected area electron diffraction (SAED) patterns, energy-dispersive X-ray spectroscopy (EDS), and, in the case of LiGaSe_2 nanocrystals, ^7Li , ^{69}Ga , and ^{77}Se solid state (SS) NMR analysis, confirms the identity and phase purity of the different crystalline materials. All nanocrystals except NaIn_3Te_5 are photoluminescent, with modest PL QYs between 1.2% and 4.6%.

Critically, we can selectively isolate either of the tetragonal (chalcopyrite) (*I42d*) or orthorhombic (*Pna2₁*) phases of LiGaSe_2 and LiInSe_2 nanocrystals using different dichalcogenide (RSeSeR) precursors. Specifically, highly reactive EtSeSeEt yields the most stable, thermodynamic *I42d* phase while mildly reactive PhSeSePh yields the metastable (kinetic) *Pna2₁* phase. Density functional theory (DFT) calculations on both compositions confirm the relative energy order between these polymorphs—separated by only 2.7–6.4 meV per formula units—as well as other, higher energy phases in the case of LiInSe_2 . Further, DFT predicts a powder XRD pattern of a previously unreported, *C2* NaIn_3Te_5 phase that matches the powder XRD observed experimentally.

Experimental

Materials

Oleylamine (oleyl NH_2 , 70%), 1-octadecene (ODE, 90%), diphenyl diselenide (98%), diphenyl ditelluride (98%), and indium(III) acetylacetonate (99.99+% In) were purchased from Sigma-Aldrich; gallium(III) acetylacetonate (99.99+% Ga), indium(III) acetylacetonate (99.99+% In), lithium acetylacetonate (99.99+% Li), and sodium oleate (99%) from Strem; diphenyl disulfide (99%) from Acros. **Caution:** oleylamine is very corrosive and should be handled with great care.

Synthesis of LiTrCh_2 nanocrystals

Lithium acetylacetonate (0.10 mmol, 11 mg for LiInSe_2 and LiGaSe_2 ; 0.15 mmol, 16 mg for LiInS_2) and gallium or indium acetylacetonate (0.10 mmol, 37 mg for Ga; 0.10–0.20 mmol, 41–82 mg for In) were dissolved and stirred in a mixture of oleyl NH_2 (2 mL) and ODE (4 mL) in a round-bottom (RB) flask at 100 °C for 1 h under dynamic vacuum. After refilling the RB flask with N_2 , diphenyl disulfide/diselenide (0.20–0.60 mmol, 44–131 mg for S; 0.20 mmol, 62 mg for Se) in oleyl NH_2 (2 mL) was swiftly injected. The temperature was raised to 270–330 °C, and stirring was continued for 30–60 min. The crude solution was treated with an equivalent amount of ethanol and centrifuged at

4500 rpm for 5 min. After discarding the supernatant, the precipitate containing nanocrystalline solids was redispersed in hexanes, treated with an equivalent amount of ethanol and a few drops of methanol, and centrifuged again at 4500 rpm for 5 min.

NaTrCh_2 or NaTr_3Ch_5 nanocrystals

These were synthesized in a similar procedure with sodium oleate (0.10 mmol, 37 mg), indium acetylacetonate (0.10 mmol, 37 mg), and diphenyl disulfide/diselenide/ditelluride (0.2 mmol, 44 mg for S; 0.10 mmol, 31 mg for Se; 0.05 mmol, 21 mg for Te) dissolved in oleyl NH_2 (2 mL). The reaction temperatures for specific compositions are listed in Table 1.

Structural characterization

Powder X-ray diffraction (XRD) was collected on a Rigaku Ultima IV diffractometer (40 kV, 44 mA) with a zero-background quartz sample holder using Cu K radiation. A *K* value of 0.9 was used to determine average single-crystalline domain sizes using the Scherrer equation. A JOEL JSM-IT200 scanning electron microscope was used for area scans and elemental mapping. Samples were put on double-sided carbon tape and examined at a voltage of 10–15 keV. A JEOL 2100 transmission electron microscope was utilized to carry out transmission electron microscopy imaging. Size distributions contain information from at least 100–200 particles. The samples were prepared by drop-casting a dilute nanocrystal solution in hexane on a Cu grid with a 200-mesh carbon coating.

Optical characterization

A photodiode array Agilent 8453 UV/vis spectrophotometer was used to measure the absorption spectra of the nanocrystals in solution. All spectra are reported after subtracting the absorption of the solvent. Diffuse reflectance spectra were recorded using an SL1 Tungsten Halogen lamp (vis-IR), an SL3 Deuterium Lamp (UV), and a BLACK-Comet C-SR-100 spectrometer (200–1080 nm). Band gap values were estimated by extrapolating the linear slope of Tauc plots of $(A h\nu)^{1/r}$ versus $h\nu$ (A = absorbance, $h\nu$ = incident photon energy in eV, $r = 1/2$ for direct and $r = 2$ for indirect semiconductors).⁷⁴ A Horiba-Jobin Yvon Nanolog scanning spectrofluorometer with a photomultiplier detector was used to measure steady-state PL spectra. Rhodamine 440 or rhodamine 460 dye was utilized as a standard for measuring the relative PL quantum yields (QYs).⁷⁵ Replicates of three or more were used to measure the absorption and PL emission spectra, and the average QYs were recorded.

Solid-state NMR

SSNMR spectroscopy experiments (except ^{69}Ga) were performed on a Bruker wide-bore 9.4 T [$\nu_0(^1\text{H}) = 400$ MHz] NMR spectrometer equipped with a Bruker Advance III HD console. ^7Li SSNMR spectra were acquired with a Bruker 4 mm HX MAS probe configured in ^1H - ^7Li mode. A rotor-synchronized spin-echo pulse sequence was used with 62.5 kHz radio frequency (RF), CT-selective pulses. 3072 scans (LiGaSe_2) or 300 scans



(LiInSe₂) were acquired with a 2 s recycle delay between scans. The MAS frequency was 10 kHz. ⁷⁷Se SSNMR spectra were acquired with a Bruker 2.5 mm HX MAS probe configured in ¹H-⁷⁷Se mode. A rotor-synchronized spin-echo pulse sequence was used with 83.3 kHz radio frequency (RF), CT-selective pulses. 560 scans were acquired with a 100 s recycle delay between scans and 23 CPMG loops. The MAS frequency was 22 kHz. ⁶⁹Ga SSNMR experiments were performed on a Bruker wide-bore 14.1 T [$\nu_0(^1\text{H}) = 600 \text{ MHz}$] NMR spectrometer equipped with a Bruker Advance NEO console, WCPMG pulse sequence with a 1 s delay, 25 ms WURST pulse, 12 CPMG loops, 40 960 with a Bruker 4 mm HX MAS probe configured in ¹H-¹¹⁵In mode. Peak fitting of the SSNMR spectra was performed in the solid line-shape analysis module version 3.6.3 included in the Bruker Topspin version 3.6.5 software. ¹H chemical shifts were referenced to tetramethylsilane by using adamantane [$\delta_{\text{iso}}(^1\text{H}) = 1.82 \text{ ppm}$] as a secondary chemical shift standard. ⁷Li, ⁶⁹Ga, and ⁷⁷Se chemical shifts were referenced indirectly to the established chemical shift scale [LiCl, $\delta_{\text{iso}}(^7\text{Li}) = 0 \text{ ppm}$], [Ga(NO₃)₂, $\delta_{\text{iso}}(^{69}\text{Ga}) = 0 \text{ ppm}$], [SeMe₂, $\delta_{\text{iso}}(^{77}\text{Se}) = 0 \text{ ppm}$] using the previously published relative NMR frequencies.⁷⁶

Electronic structure calculations

Calculations were carried out using the Vienna *Ab initio* Simulation Package (VASP)⁶⁵ and the Tight Binding Linear Muffin-tin Orbital Atomic Sphere Approximation (TB-LMTO-ASA) package.⁶⁶ PBE band structures and DOS were calculated using the tetrahedron method after converging the total energy on a *k*-mesh of $1/a \times 1/b \times 1/c$ in the irreducible wedge of the Brillouin zone. Unit cell representations were generated using VESTA.⁷⁷

Author contributions

Md Riad Sarkar Pavel: writing – original draft, conceptualization, methodology, synthesis and computational investigation. Anuluxan Santhiran: solid-state NMR investigation, methodology. Seth Dalberg: synthesis investigation, methodology. Aaron J. Rossini: solid state NMR and writing – review & editing. Javier Vela: supervision, writing – review & editing.

Conflicts of interest

There are no conflicts to declare.

Data availability

Supplementary information: powder XRD, electron microscopy images, SS NMR measurements, and DFT calculations. See DOI: <https://doi.org/10.1039/d5ta07992f>.

Acknowledgements

This invited manuscript is dedicated to celebrating Prof. D. D. Sarma's contributions to materials science. This work was supported by the U.S. National Science Foundation, Division of Chemistry, Macromolecular, Supramolecular, and

Nanochemistry Program (2305062) by a grant awarded to J. V. SSNMR work by A. S. and A. J. R. was supported by the U.S. Department of Energy (DOE) Ames National Laboratory, Materials Science and Engineering Division. Ames National Laboratory is operated for the U.S. DOE by Iowa State University, under contract no. DE-AC02-07CH11358. We thank Gordie Miller and Federico Zahariev for discussions.

References

- 1 J. L. Dye, *Philos. Trans. R. Soc. A*, 2015, **373**, 20140174.
- 2 Y. Shen, Z. Zhu, Z. Xu and Y. Li, *Energy Adv.*, 2024, **3**, 1844–1868.
- 3 H. Hao, T. Hutter, B. L. Boyce, J. Watt, P. Liu and D. Mitlin, *Chem. Rev.*, 2022, **122**, 8053–8125.
- 4 P. Xu, F. Huang, Y. Sun, Y. Lei, X. Cao, S. Liang and G. Fang, *Adv. Funct. Mater.*, 2024, **34**, 2406080.
- 5 A. Kausar, A. Sattar, C. Xu, S. Zhang, Z. Kang and Y. Zhang, *Chem. Soc. Rev.*, 2021, **50**, 2696–2736.
- 6 A. Van der Ven, Z. Deng, S. Banerjee and S. P. Ong, *Chem. Rev.*, 2020, **120**, 6977–7019.
- 7 Y. Zhang, R. Cao, C. Ouyang, L. Jiang, Y. Wang, M. Yang and H. Xia, *J. Mater. Chem. A*, 2025, **13**, 3973–3990.
- 8 F. Wu, J. Maier and Y. Yu, *Chem. Soc. Rev.*, 2020, **49**, 1569–1614.
- 9 F. Zhang, B. He, Y. Xin, T. Zhu, Y. Zhang, S. Wang, W. Li, Y. Yang and H. Tian, *Chem. Rev.*, 2024, **124**, 4778–4821.
- 10 T. Hosaka, K. Kubota, A. S. Hameed and S. Komaba, *Chem. Rev.*, 2020, **120**, 6358–6466.
- 11 Y. Zhang, B. Han, S. Tan, Q. Gao, Z. Cai, C. Zhou, J. Li, R. Sun and K. Amine, *Adv. Energy Mater.*, 2025, **15**, 2404796.
- 12 H. McKeever, N. N. Patil, M. Palabathuni and S. Singh, *Chem. Mater.*, 2023, **35**, 9833–9846.
- 13 C. A. Aranda, A. O. Alvarez, V. S. Chivrony, C. Das, M. Rai and M. Saliba, *Joule*, 2024, **8**, 241–254.
- 14 A. Karami, M. Morawski, H. Kempa, R. Scheer and O. Cojocar-Mirédin, *Sol. RRL*, 2024, **8**, 2300544.
- 15 B. A. Tappan and R. L. Brutchey, *ChemNanoMat*, 2020, **6**, 1567–1588.
- 16 M. A. White, A. M. Medina-Gonzalez and J. Vela, *Chem.–Eur. J.*, 2018, **24**, 3650–3658.
- 17 H. Dong, J. Zhao, H. Yang and Y. Zheng, *Phys. Rev. Mater.*, 2022, **6**, 104001.
- 18 L. I. Isaenko and A. P. Yelissev, *Semicond. Sci. Technol.*, 2016, **31**, 12300.
- 19 N. Jia, S. Wang, P. Wang, C. Li, T. Yu, J. Qiao, C. Li, X. Xiong, J.-L. Sun and X. Tao, *J. Mater. Chem. C*, 2018, **6**, 12615–12622.
- 20 T. V. Vu, A. A. Lavrentyev, B. V. Gabrelian, D. D. Vo, P. D. Khang, L. I. Isaenko, S. I. Lobanov, A. F. Kurus and O. Y. Khyzhun, *RSC Adv.*, 2020, **10**, 26843–26852.
- 21 Y. Fan, X. Song, S. Qi, X. Ma and M. Zhao, *J. Mater. Chem. A*, 2019, **7**, 26123–26130.
- 22 T. Biswas and A. K. Singh, *npj Comput. Mater.*, 2021, **7**, 189.
- 23 Z. Zheng, H. Yu, M. Zhu, Z. Zhang, Z. Gao, M. Xu, R. Zhang and Y. Xu, *Sci. Rep.*, 2024, **14**, 24779.
- 24 Z. Liu, Y. Sun, D. J. Singh and L. Zhang, *Adv. Electron. Mater.*, 2019, **5**, 1900089.



- 25 Y. Zhao, L. Huang, D. Zhao and J. Yang Lee, *Angew. Chem., Int. Ed.*, 2023, **62**, 202308976.
- 26 W. Hua, H. Li, C. Pei, J. Xia, Y. Sun, C. Zhang, W. Lv, Y. Tao, Y. Jiao, B. Zhang and S. Z. Qiao, *Adv. Mater.*, 2021, **33**, 2101006.
- 27 J. Yang, X. Huang, X. Xu, H. Lu, S. Wang and S. Wu, *ACS Appl. Mater. Interfaces*, 2024, **16**, 15050–15058.
- 28 V. Bikbaeva, O. Perez, N. Nesterenko and V. Valtchev, *Inorg. Chem. Front.*, 2022, **9**, 5181–5187.
- 29 J. De Roo, *Chem. Mater.*, 2022, **34**, 5766–5779.
- 30 M. A. White, K. J. Baumler, Y. Chen, A. Venkatesh, A. M. Medina-Gonzalez, A. J. Rossini, J. V. Zaikina, E. M. Chan and J. Vela, *Chem. Mater.*, 2018, **30**, 6173–6182.
- 31 Y. Guo, S. R. Alvarado, J. D. Barclay and J. Vela, *ACS Nano*, 2013, **7**, 3616–3626.
- 32 M. P. Hendricks, M. P. Campos, G. T. Cleveland, I. Jen-La Plante and J. S. Owen, *Science*, 2015, **348**, 1226–1230.
- 33 M. R. S. Pavel, A. Santhiran, S. Dalberg, A. J. Rossini and J. Vela, *ACS Nano*, 2025, **19**, 33413–33422.
- 34 M. R. S. Pavel, Y. Chen, A. Santhiran, E. Gi, K. Ochoa-Romero, G. J. Miller, G. Guirado, A. J. Rossini and J. Vela, *ACS Energy Lett.*, 2024, **9**, 5012–5018.
- 35 B. A. Tappan, G. Barim, J. C. Kwok and R. L. Brutchey, *Chem. Mater.*, 2018, **30**, 5704–5713.
- 36 E. J. Endres, J. R. Bairan Espano, A. Koziel, A. R. Peng, A. A. Shults and J. E. Macdonald, *ACS Nanosci. Au*, 2024, **4**, 158–175.
- 37 Y. Fu, X. Duan, M. Xing, N. Zhang, X. Luo, H. Wang and Y. Ma, *Mater. Lett.*, 2014, **124**, 141–143.
- 38 A. Adhikary, H. Yaghoobnejad Asl, P. Sandinini, S. Balijapelly, S. Mohapatra, S. Khatua, S. Konar, N. Gerasimchuk, A. V. Chernatynskiy and A. Choudhury, *Chem. Mater.*, 2020, **32**, 5589–5603.
- 39 V. V. Klepov, A. A. Berseneva, K. A. Pace, V. Kocovski, M. Sun, P. Qiu, H. Wang, F. Chen, T. M. Besmann and H. C. Zur Loye, *Angew. Chem., Int. Ed.*, 2020, **59**, 10836–10841.
- 40 S. F. Li, X. M. Jiang, B. W. Liu, D. Yan, C. S. Lin, H. Y. Zeng and G. C. Guo, *Chem. Mater.*, 2017, **29**, 1796–1804.
- 41 Z. Sun, C. M. Perez, O. V. Prezhdo and R. L. Brutchey, *ACS Nanoscience Au*, 2024, **4**, 381–390.
- 42 Z. Sun, C. P. Pakhanyan, U. Saleem, E. I. Feldman, S. Mallikarjun Sharada and R. L. Brutchey, *Inorg. Chem.*, 2025, **64**, 21796–21800.
- 43 S. K. O'Boyle, A. Naeem and R. E. Schaak, *Chem. Mater.*, 2025, **37**, 8889–8900.
- 44 H. Yan, L. Chen, L. Feng, Y. Chen, M. Zhang and Q. Wei, *Vacuum*, 2024, **225**, 113256.
- 45 R. F. Ali and B. D. Gates, *Nanoscale*, 2021, **13**, 3214–3226.
- 46 C.-Y. Yeh, Z. Lu, S. Froyen and A. Zunger, *Phys. Rev. B: Condens. Matter Mater. Phys.*, 1992, **46**, 10086–10097.
- 47 Y. E. Maidebura, V. G. Mansurov, T. V. Malin, I. A. Aleksandrov, K. S. Zhuravlev and B. Pecz, *CrystEngComm*, 2025, **27**, 2307–2316.
- 48 N. Kapuria, B. Nan, T. E. Adegoke, U. Bangert, A. Cabot, S. Singh and K. M. Ryan, *Chem. Mater.*, 2023, **35**, 4810–4820.
- 49 M. Strach, V. Mantella, J. R. Pankhurst, P. Iyengar, A. Loiudice, S. Das, C. Corminboeuf, W. van Beek and R. Buonsanti, *J. Am. Chem. Soc.*, 2019, **141**, 16312–16322.
- 50 R. K. Harris, E. D. Becker, S. M. Cabral de Menezes, R. Goodfellow and P. Granger, *Pure Appl. Chem.*, 2001, **73**, 1795–1818.
- 51 S. E. Ashbrook, *Phys. Chem. Chem. Phys.*, 2009, **11**, 6892–6905.
- 52 S. E. Ashbrook and S. Sneddon, *J. Am. Chem. Soc.*, 2014, **136**, 15440–15456.
- 53 R. W. Schurko, *Acc. Chem. Res.*, 2013, **46**, 1985–1995.
- 54 L. A. O'Dell, A. J. Rossini and R. W. Schurko, *Chem. Phys. Lett.*, 2009, **468**, 330–335.
- 55 W. H. Dawson and J. D. Odom, *J. Am. Chem. Soc.*, 1977, **99**, 8352–8354.
- 56 J. D. Odom, W. H. Dawson and P. D. Ellis, *J. Am. Chem. Soc.*, 1979, **101**, 5815–5822.
- 57 A. Eifler, V. Riede, J. Brückner, S. Weise, V. Krämer, G. Lippold, W. Schmitz, K. Bente and W. Grill, *Jpn. J. Appl. Phys.*, 2000, **39**, 279.
- 58 L. Isaenko, I. Vasilyeva, A. Yelisseyev, S. Lobanov, V. Malakhov, L. Dovlitova, J. J. Zondy and I. Kavun, *J. Cryst. Growth*, 2000, **218**, 313–322.
- 59 M. Jomaa, V. Mishra, D. Mumbaraddi, R. Sikdar, D. Sarkar, M. Sun, J. Yao, V. K. Michaelis and A. Mar, *Inorg. Chem.*, 2023, **62**, 7491–7502.
- 60 D. Clark, J. Zhang, A. Craig, A. Weiland, J. Brant, J. Cho, Y. Kim, J. Jang and J. Aitken, *J. Alloys Compd.*, 2022, **917**, 165381.
- 61 E. Tupitsyn, P. Bhattacharya, E. Rowe, L. Matei, Y. Cui, V. Buliga, M. Groza, B. Wiggins, A. Burger and A. Stowe, *J. Cryst. Growth*, 2014, **393**, 23–27.
- 62 L. Isaenko, A. Yelisseyev, S. Lobanov, V. Petrov, F. Rotermund, G. Slekyš and J.-J. Zondy, *J. Appl. Phys.*, 2002, **91**, 9475–9480.
- 63 L. Guo, Y. Xu, H. Zheng, W. Xue, J. Dong, B. Zhang, Y. He, G. Zha, D. Y. Chung, W. Jie and M. G. Kanatzidis, *Cryst. Growth Des.*, 2018, **18**, 2864–2870.
- 64 A. K. P. Mann, S. Wicker and S. E. Skrabalak, *Adv. Mater.*, 2012, **24**, 6186–6191.
- 65 G. Kresse and J. Furthmüller, *Comput. Mater. Sci.*, 1996, **6**, 15–50.
- 66 O. Jepsen, A. Burkhardt and O. K. Andersen, *The Program TB-LMTO-ASA*, version 4.7, Max-Planck-Institut für Festkörperforschung, Stuttgart, Germany, 1999.
- 67 G. J. Miller, *Eur. J. Inorg. Chem.*, 1998, **1998**, 523–536.
- 68 B. A. Rosales, M. A. White and J. Vela, *J. Am. Chem. Soc.*, 2018, **140**, 3736–3742.
- 69 P. Mori-Sánchez, A. J. Cohen and W. Yang, *Phys. Rev. Lett.*, 2008, **100**, 146401.
- 70 A. A. Lavrentyev, B. V. Gabrelian, V. T. Vu, L. N. Ananchenko, L. I. Isaenko, A. P. Yelisseyev and O. Y. Khyzhun, *Opt. Mater.*, 2017, **66**, 149–159.
- 71 W. Chen, J. M. Zhang, Q. L. Xia, Y. Z. Nie and G. H. Guo, *Phys. Chem. Chem. Phys.*, 2020, **22**, 16007–16012.
- 72 M. S. Khan, B. Gul, G. Khan, S. A. Khattak, M. Ajaz, T. Khan and S. Zulfiqar, *J. Solid State Chem.*, 2022, **307**, 122853.



- 73 W. B. Cai, A. Abudurusuli, C. W. Xie, E. Tikhonov, J. J. Li, S. L. Pan and Z. H. Yang, *Adv. Funct. Mater.*, 2022, **32**, 2200231.
- 74 B. D. Viezbicke, S. Patel, B. E. Davis and D. P. Birnie, *Phys. Status Solidi B*, 2015, **252**, 1700–1710.
- 75 M. Grabolle, M. Spieles, V. Lesnyak, N. Gaponik, A. Eychmüller and U. Resch-Genger, *Anal. Chem.*, 2009, **81**, 6285–6294.
- 76 R. K. Harris, E. D. Becker, S. M. Cabral de Menezes, R. Goodfellow and P. Granger, *Solid State Nucl. Magn. Reson.*, 2002, **22**, 458–483.
- 77 K. Momma and F. Izumi, *J. Appl. Crystallogr.*, 2011, **44**, 1272–1276.

